ADVANCED MATERIALS INTERFACES
www.advmatinterfaces.de

Comparative Internal Pressure Evolution at Interfaces of Activated Carbon for Supercapacitors Containing Electrolytes Based on Linear and Cyclic Ammonium Tetrafluoroborate Salts in Acetonitrile

*Georgios Nikiforidis, Satyajit Phadke, and Mérièm Anouti**

In this study, the real-time increase in pressure of the accumulated gases at the electrode/electrolyte interface serves as a safety criterion for four conductive electrolytes comprising acetonitrile (ACN) and organic salts. They include tetrafluoroborate as an anion and cyclic 1,1-dimethylpyrrolidinium ($Pyr11^+$), spiro-(1,1′)-bipyrrolidinium (SBP^+), acyclic methyl triethyl ammonium (Et_3MeN^+) or standard tetraethylammonium (Et_4N^+) as cations. The main focus lies on the $SPBF_4$/ACN system. While the concentrated $Pyr11BF_4$/ACN exhibits a minimal pressure evolution (≈25 Pa) under ambient conditions at 3.0 V, its electrochemical stability is inferior to $SPBF_4$ at high operating voltage. The electrolytes with acyclic tetrafluoroborate salts (1.0 mol L^{-1}) reveal a 20-fold increase in pressure due to the weak salt-ACN interactions and the subsequent high solvent evaporation. The pressure evolution at the interface of activated carbon/electrolyte in electrochemical double layer capacitor (EDLCs) is merely related to the operating voltage and cation nature, viz. $Pyr11^+ < SBP^+ < Et_4N^+ < Et_3MeN^+$. The fixed specific capacity of 109 F g^{-1}, volumetric capacity of 76 F cm^{-3}, and moderate gas generation (≈190 Pa at 3.0 V, that shifts to ≈400 Pa at 3.4 V) confirm the safe character of the $SPBF_4$/ACN electrolyte for such energy storage devices.

1. Introduction

A symmetric cell design featuring identical positive and negative electrodes is referred to as an electric double-layer capacitor (EDLC), where the prevalent mechanism entails non-Faradaic charge storage at the interface between a high surface area material and a liquid electrolyte. These energy storage devices are intriguing due to their high power density (10 kW kg^{-1}), rapid response time (1 s), cycle-life (10^5 cycles) and safety.[1] Nanoporous carbon materials are commonly used in EDLCs. Their porous structures act as a bulk buffering reservoir for any medium, curtailing the ion transport resistance to the interior surface of the pores.[2] Increased pore accessibility caters to a larger number of cations to populate the electrode's double layer, leading to specific capacitances of the order of 200 F g^{-1}, as is for the case of activated carbon.[3] The latter is widely used in these energy storage devices as it is inexpensive, i.e., the carbonization process originates from wood, coal, and nutshell and is easily prepared compared with other porous materials such as templated carbons and carbide-derived carbons. With a specific surface area of ≈2000 m^2 g^{-1}, it can provide ≈30 mAh g^{-1} V^{-1} counter to 150 mAh g^{-1} V^{-1} for standard battery electrodes.[4,5]

Typically, the electrochemical window of EDLCs is lower than that of batteries (e.g., 4.3 V for nickel manganese oxide-graphite battery). Thus, as the energy stored is proportional to the square root of the voltage (E_{EDLC} = ½ C × V^2; C denotes capacitance and V voltage), their energy density is hindered, i.e., E_{LIB} = 3-30 × E_{EDLC}. It should be noted that E_{EDLC} hinges on the nature of the double layer, that is, the specific Helmholtz compact layer geometry, the size of electrolyte cations and anions, their degree of solvation, and the orientation of the electrolyte solvent dipoles in the imposed electric field.[6] Accordingly, organic electrolytes are an attractive choice as they can reach operating voltages as high as 3.5 V. Acetonitrile (ACN) is a representative dipolar aprotic solvent that boasts operating temperatures at sub-zero range ($T_{melting\ ACN}$ = −45 °C), fluidity (η = 0.345 mPa s^{-1} at 25 °C), a large operating voltage window (>3.0 V),[7] low internal resistance, facile ionic adsorption within the pores of carbon-based electrodes and electrochemical stability due to its low viscosity and high dielectric constant (ε = 38)

G. Nikiforidis
Institute for Materials Discovery
University College London
Malet Place, London WC1E 7JE, UK
S. Phadke, M. Anouti
Laboratoire PCM2E
Université de Tours
Parc de Grandmont
Tours 37200, France
E-mail: meriem.anouti@univ-tours.fr
The ORCID identification number(s) for the author(s) of this article can be found under https://doi.org/10.1002/admi.202202046.

DOI: 10.1002/admi.202202046

Table 1. Cation and anion structures of the investigated ammonium tetrafluoroborate salts together with the Lennard-Jones parameters calculated by ab initio Hartree-Fock calculations with the 6-31G(d) basis set for ions.

	Linear cation		Anion	Cyclic and bicyclic cation	
Structure	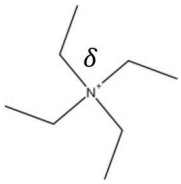	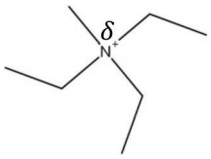	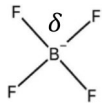	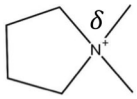	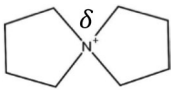
Abbreviation	Et_4N^+	Et_3MeN^+	BF_4^-	$Pyrr11^+$	SBP^+
Size (nm)[13]	0.304	0.295	0.232	0.339	0.323
Electrostatic potential	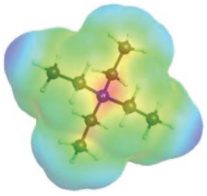	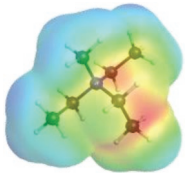	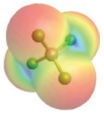	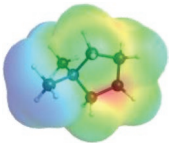	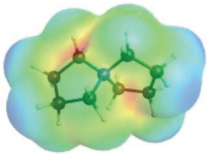
Partial charge, δ	0.088	0.144	-0.397	0.227	0.130
Dipole moment, μ (Debye)	0.001	0.922	0.001	2.165	0.724

On top of selecting the appropriate solvent for EDLC applications, the choice of salt is equally important. Quaternary ammonium salts are eligible for use in non-aqueous solutions by virtue of their facile synthesis, inexpensive production, and electrochemical stability.[8] Spiro-(1,1′)-bipyrrolidinium tetrafluoroborate ($SPBF_4$) is the most prominent quaternary ammonium salt as it is highly soluble (4.4 mol L^{-1} in acetonitrile at 25 °C[9]), possesses high ionic conductivity (e.g., 54.9 mS cm^{-1} at 2.0 mol L^{-1}) and is less sensitive against moisture.[10] Prior work has uncovered that $SPBF_4$ provides a wider operating voltage range in pure ACN than standard linear quaternary ammonium salts based on triethylammonium (Et_3N) and triethylmethylammonium (Et_3MeN) cations.[11] Besides, $SPBF_4$ in ACN exhibits a marginally higher conductivity (54.9 mS cm^{-1} at 2.0 mol L^{-1}) than Et_4NBF_4 (54.2 mS cm^{-1} at 1.6 mol L^{-1}) and $DMPBF_4$ (1,1-dimethylpyrrolidinium tetrafluoroborate) in the same medium (52.5 mS cm^{-1} at 2.0 mol L^{-1}), sufficiently high for use in EDCLs.[12]

The SBP^+ has two symmetric five-membered rings joined together by an N^+ functionality (**Table 1**). The twisted flat ring structure of SBP is advantageous for the formation of the electrochemical double layer (EDL) and the migration of ions on the surface of the electrode. In addition, tetrafluoroborate (BF_4^-) is of interest for EDLCs since it has a small ion size[13] and can operate within an elongated electrochemical window.[9] The specific capacitance of such energy storage devices relies on the size of the cation, namely Et_4NBF_4, $SPBF_4$, and $DMPBF_4$, with their radii sizes being 0.339 (Et_4N^+), 0.323 (SBP^+), and 0.304 nm (DMP^+), respectively[9] (Table 1). Small cations can easily diffuse into the micropores of the electrode(s) during adsorption and desorption, boosting the accessible surface area.[8] Their specific capacitance increases markedly when the electrode pore size is smaller than 10 Å.[14] A projected volumetric capacitance of 77 F cm^{-3} arises from the volume of AC mesopores of 0.7 cm^3 g^{-1} while the calculated specific capacitance obtained by galvanostatic charge-discharge cycling reaches 110 F g^{-1}. Table 1 also underlines the multitude of the values of partial charge, δ, electrostatic potential and dipole moment, μ, of the investigated anion and cation structures, stemmed from ab-initio Hartree-Fock calculations.

Numerous electrolytes containing stable organic salts and ACN have been reported. Examples include axoniaspiro[3,4] octane tetrafluoroborate ($APBF_4$),[15–17] tetramethylammonium tetrafluoroborate,[18] tetraethylammonium tetrafluoroborate,[19] and tetrabutylammonium tetrafluoroborate.[20] Yet, aside from their electrochemical and physical properties, their safety, reflected by the increased pressure of the accumulated gases, is just as important. This in situ technique represents a powerful tool for understanding the interplay between electrolytes and carbonaceous materials. Gas evolution is contingent on the choice of carbon, salt, and solvent. Despite various efforts to improve the quality of carbon (e.g., high-temperature hydrogen treatment to mitigate surface-oxygen bonds, elevated-temperature vacuum drying of the electrodes and the separator), EDLC contaminant concentrations remain sufficient to generate gas. Regarding the solvent, gaseous decomposition products from non-aqueous electrolytes (e.g., ACN, PC) include hydrogen, ethene, propene, carbon monoxide, carbon dioxide, metaboric acid, and alkylboranes.[16] While the last two are related to the salt (e.g., Et_4NBF_4, Et_3MeNBF_4), most of the gas evolution stems from solvent decomposition (e.g., hydrolysis of solvents in the negative compartment or electrochemical oxidation of solvent and carbon surface functional groups),[21–23] with ACN being more prone to gas evolution than propylene carbonate (PC).[24]

With the above in mind, after determining the physicochemical and electrochemical properties of the $SPBF_4$/ACN electrolyte against other conductive ACN-based analogues (Table 1), we perform comparative in situ measurements of accumulated gas pressure during typical galvanostatic charge-discharge cycles for the first time at elongated positive (oxidative) voltages and

monitor the pressure evolution under ambient conditions. The EDLC containing $Pyr11BF_4$, described as an organic ionic plastic crystal[25,26] exhibited a meagre pressure increase (≈25 Pa) compared to others with asymmetric and acyclic tetrafluoroborate (i.e., >≈500 Pa). However, the superior electrochemical performance of the device comprising 1.0 mol L^{-1} $SPBF_4$ (C_{sp} = 109 F g^{-1}) and its moderate gas generation (≈190 Pa) render it a safe and more pragmatic energy storage device.

2. Experimental Section

2.1. Electrolyte Formulation

Spiro-(1,1′)-bipyrrolidinium tetrafluoroborate ($SPBF_4$), tetraethylammonium tetrafluoroborate (Et_4NBF_4), 3-ethyl-methylammonium tetrafluoroborate (Et_3MeNBF_4), cyclic 1,1 -dimethylpyrrolidinium ($Py11BF_4$), and acetonitrile (ACN) were purchased from Sigma-Aldrich and used as received. The water content of the formulated electrolytes was determined by a Karl-Fisher coulometer (Metrohm). The electrolytes were prepared in a glovebox (Braun), where the moisture and water content was 0.1 ppm.

2.2. Physicochemical Characterization

The ionic conductivity measurements were performed with a multichannel conductivity meter (BioLogic, France) based on a frequency response analyser (MCM 10) connected to a Peltier-based temperature control unit with ten slots (WTSH 10, Biologic). The measurements were conducted between –10 and 60 °C (±0.02 °C) in sealed cells with Pt parallel-plate electrodes protecting the samples from air exposure. The viscosity and density measurements were carried out between 10 and 50 °C (±0.02 °C) using an Anton Parr coupled densitometer/viscometer equipped with a digital vibrating tube densitometer and a rolling-ball viscometer (Lovis 2000 M/ME). The densitometer/viscometer was precalibrated with ultra-pure water. The uncertainty of the measurements was 2×10^{-5} g cm^{-3} for the density and 2% for the viscosity and ionic conductivity.

2.3. EDLC Components

Activated carbon (Blue Solution, France) was the electrode of choice for the EDLCs. The porous texture of the activated carbon electrodes was analyzed by nitrogen adsorption-desorption at 77 K using an Accelerated Surface Area and Porosimetry analyzer (ASAP 2020-Micromeritics, USA). The BET surface area reached 1887 m^2 g^{-1} (the surface area based on the density functional theory S_{DFT} = 1511 m^2 g^{-1})[27] and it displayed a significant amount of mesopores (V_{meso} = 0.691 cm^3 g^{-1}) with a diameter ranging from 2 to 50 nm (Figure S1, Table S1, Supporting Information). The electrodes comprised AC/polyvinylidene difluoride/carbon black at an 80/10/10 wt (weight) ratio. The average loading of AC per unit area was 5 mg cm^{-2} (on an aluminium current collector) and the bulk density reached 0.7 cm^3 g^{-1}. The cells were assembled in an argon-filled glove box with oxygen and water contents of 0.1 ppm. A Whatman GF/C glass microfiber filter (thickness of 675 mm) was used as the separator. The quantity of electrolytes added to each cell was 150 µL.

Cyclic voltammetry (in an electrolyte consisting of $SPBF_4$ and ACN) was performed to equilibrate the mass loading of the positive and negative electrodes (Figure S2, Supporting Information). They were balanced subject to the electrochemical stability limits and the specific capacitance of the device to avoid premature ageing. After equilibrating the mass loadings, a negative (ϕ = 10 mm) and a positive (ϕ = 12 mm) electrode were used for the cell assembly. Prior to the electrochemical testing, a 12 h conditioning process was commissioned.

2.4. Electrochemical Testing of EDLCs

Galvanostatic charge-discharge cycling (GCD), accelerated ageing floating tests, cyclic voltammetry (CV), and potentiostatic impedance spectroscopy (PEIS) were carried out in Swagelok cells by a computer-controlled multichannel potentiostat/galvanostat (VMP3, Biologic, France). The floating protocol was initiated with five initial GCD cycles at a normalized current density of 1.75 A g^{-1} (normalized with respect to the mass of the activated carbon, 5.0 mg), followed by a constant voltage step at 3.0 V for 1.5 h and followed by further five GCD cycles. This sequence was repeated for 125 h. CV was performed relative to the set electrochemical window at designated scan rates (i.e., 1–100 mV s^{-1}). PEIS was conducted between 0.1 MHz and 10 mHz (ten points per decade) at open-circuit voltage with an oscillating amplitude fixed at 10 mV. The quality of the EIS spectra was validated through the Kramers-Kronig test. All EDLC devices were cycled under ambient conditions. The data presented are the average values of three separate trials.

2.5. In Situ Gas Pressure Measurements of the EDLCs

The in-situ gas pressure measurements followed a methodology described in previous studies.[28–30] They were performed in an ECC-Press-Air-DL cell (EL-CELL, Germany) equipped with an inlet probe connected to pressure and temperature sensors that simultaneously take the readings at a frequency of 10 Hz. The resolution of the temperature sensor was 0.01 °C. The sensor's pressure varied between 0 and 2.5 bar with a resolution of 1.25×10^8 Pa. The dead space in the pressure cell was ≈4.448 cm^3. To eliminate the effect of temperature on the pressure readings, the raw value of the measured pressure was corrected based on the measured temperature for each data point by assuming ideal gas behavior and taking the initial temperature (21 °C) as the reference.[23] Two separators (Whatman filter paper, GF/C, ϕ = 14 mm) were placed between the equilibrated activated carbon electrodes. The quantity of electrolyte added in the ECC-Press-Air-DL cell was 300 µL.

2.6. Ab-Initio Calculations

The Lennard-Jones parameters given by ab initio calculations followed the same theory level for all solute molecules, that is

the Hartree-Fock method with the 6-31G(d) basis set. All partial charges were obtained, while the self-consistent isodensity polarizable continuum model was implemented in Gaussian. The electrostatic potentials were based on the grid-based method scheme. The atomic charges were fitted to reproduce the molecular electrostatic potential at several points around the molecule.

3. Results and Discussion

3.1. Transport and Volumetric Properties of the Electrolyte

Figure 1 displays the conductivity, viscosity, and density variation with temperature for the $SPBF_4$/ACN and Et_4NBF_4/ACN electrolytes. Figure 1a establishes that the 1.0 mol L^{-1} $SPBF_4$/ACN electrolyte is the most conductive (40–80 mS cm^{-1}), equivalent to the 1.3 mol L^{-1} Et_4NBF_4/ACN mixture. All ions are assumed to be solvated and contribute to the electrolyte conductivity. In all solutions, the residual conductivity at low temperatures (–10 °C) reaches 40 mS cm^{-1} and is within EDLC operational limits.[12] Additionally, the $SPBF_4$/ACN electrolyte yields similar conductivities to other common cyclic or linear ammonium-based organic salts dissolved in ACN, namely $Pyrr11BF_4$ and Et_3MeNBF_4 (Figure S3, Supporting Information).

Adding salt to ACN promotes ion-solvent interactions and increases the viscosity of the formulated electrolytes, as depicted in Figure 1b. For the Et_4NBF_4/ACN solution, the viscosity rises from 0.63 to 0.83 mPa s^{-1} for a 50%-fold increase in concentration at room temperature (i.e., 1.0 → 1.5 mol L^{-1}). Still, the 1.0 mol L^{-1} Et_4NBF_4/ACN viscosity is lower than the one containing equimolar amounts of $SPBF_4$ (0.73 mPa s^{-1} at 25 °C) due to the favored solvation of the eight-ring structured cations with ACN. Despite the higher viscosity of $SPBF_4$/ACN, its ion mobility is not hindered in ACN, suggesting that the cation-anion interaction is less critical.

The compactness of the investigated electrolytes (Figure 1c, expressed in g cm^{-3}) follows the outcome of the viscosity measurements. SBP^+ is more "structure forming" than ammonium (Et_4N^+) and, at 1.0 mol L^{-1}, the former holds more free volume than its tetraethylammonium counterpart, indicating a stronger SBP^+—ACN interaction than the EtN^+—ACN one. This is obvious when considering the ionic radii and charge density (i.e., $\delta = +0.130$ and $\delta = +0.088$ nm, Table 1) of SBP^+ and Et_4N^+, respectively. Previous studies have demonstrated that the molecular interactions between ACN and the ammonium cation increase in the order of $Et_4N^+ < SBP^+$, supported by their solvation free energy values ($\Delta G_{solvation}$), i.e., Et_4N^+—ACN (–184.5 kJ mol^{-1}) and SBP^+—ACN (–191.3 kJ mol^{-1}), respectively.[9]

The viscosity and conductivity variations with temperature are modelled by the Arrhenius equation (Equations (1) and (2), Figure 1d,e) and give insight into the activation energies of viscous flow (E_a^η) and ionic mobility (E_a^σ).

$$\ln(\eta) = \ln(\eta 0) + \frac{E_a^\eta}{RT} \quad (1)$$

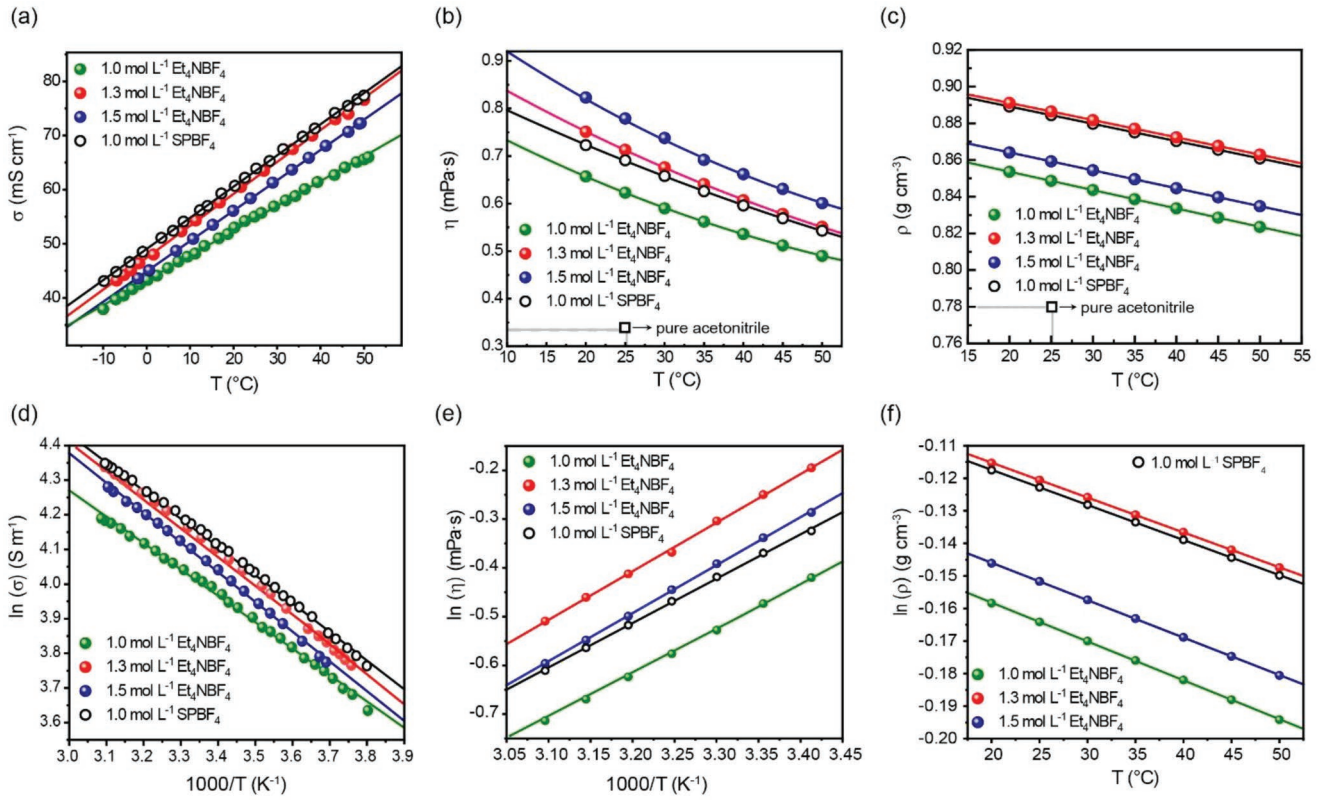

Figure 1. Evolution of a) conductivity, b) viscosity, and c) density of the Et_4NBF_4/ACN and $SPBF_4$/ACN electrolytes with temperature. Arrhenius model fittings based on d) conductivity and e) viscosity. f) Evaluation of the thermal coefficient of expansion of liquids, α.

Table 2. Summary of the transport and volumetric properties of the Et_4NBF_4/ACN and $SPBF_4$/ACN electrolytes. The activation energies (E_a^σ, E_a^η) from the Arrhenius model fitting and the coefficient of thermal expansion (α) are presented. The coefficient of thermal expansion of acetonitrile is $\approx\alpha \times 10^3$ (K^{-1}) = 1.397.[35] *denotes this work.

Electrolyte salt in ACN	η [mPa s]			σ [mS cm^{-1}]			ρ [g cm^{-3}]		
	20 °C	50 °C	E_a^η [kJ mol^{-1}]	20 °C	50 °C	E_a^σ [kJ mol^{-1}]	20 °C	50 °C	$\alpha \times 10^3$ [K^{-1}]
1.5 mol L^{-1} Et_4NBF_4	59.5	77.1	8.28	0.82	0.60	7.23	0.89	0.86	–1.19
1.3 mol L^{-1} Et_4NBF_4	56.1	72.3	8.19	0.74	0.55	7.15	0.86	0.83	–1.15
1.0 mol L^{-1} Et_4NBF_4	53.4	65.0	7.70	0.65	0.48	6.50 * 6.50[36]	0.55	0.82	–1.07
1.0 mol L^{-1} $SPBF_4$	60.0	78.2	7.56	0.72	0.54	6.90 * 6.40[36]	0.55	0.82	–1.08

$$\ln(\sigma) = \ln(\sigma_0) - \frac{E_a^\sigma}{RT} \quad (2)$$

where R, and T, are the universal gas constant (8.314 J mol^{-1} K^{-1}) and absolute temperature, η_0 and σ_0 are the fitting parameters. The fitted plots of the viscosities and conductivities as a function of temperature at different concentrations from 1.0 to 1.5 mol L^{-1} follow the Arrhenius behavior,[31,32], i.e., they are linearly correlated (correlation coefficient $R^2 > 0.995$). The activation energies E_a^σ, E_a^η extracted from slopes at different salt concentrations are summarized in **Table 2** and are on par with the literature.[9] The ionic mobilities (E_a^σ) increase with higher Et_4NBF_4 concentrations and are slightly lower (≈1 kJ mol^{-1}) than the activation energies of viscous flow (E_a^η). This difference is ascribed to solvent-solvent interactions that are not taken into account in ion mobility, as opposed to the viscous flow's energy barrier. The coefficient of thermal expansion of liquid electrolytes, α, determines the swelling rates of electrolytes during temperature variations, such as in this case, viz., –60 to 50 °C. It can be evaluated from the linear fitting of the temperature-density data (Figure 1f) through the following equation:

$$\ln(\rho) = \beta - \alpha T(K) \quad (3)$$

where ρ is the density, β a constant, and α the coefficient of thermal expansion. The values obtained here are in the same range (i.e., 1×10^3 K^{-1}) as the ones comprising fluoroethylene carbonate-based solvent mixtures and lithium bis(trifluoromethanesulfonyl)-imide (LiTFSI)[33] or lithium hexafluorophosphate ($LiPF_6$).[34] With increasing Et_4NBF_4 amounts, a divergence of the volumetric expansion coefficients is observed (e.g., $1.19 \rightarrow 1.07 \times 10^3$ K^{-1}). Overall, at a salt concentration of 1.0 mol L^{-1} the E_a^σ, E_a^η and α values are comparable for the studied ACN-based electrolytes.

3.2. Electrochemical Characterization of AC-Based Symmetric EDLCs

Figure 2a compares the electrochemical performance of EDLCs under common conductive electrolytes like Et_3MeNBF_4 and Et_4NBF_4 in ACN (Figure S2, Supporting Information) with the ones containing $SPBF_4$ and concentrated $Pyrr11BF_4$ in the same medium. The salt concentration is ≈1.0 mol L^{-3}. Aside from the $Pyrr11BF_4$, the cyclic voltammograms of the other electrolytes yield a rectangular shape, indicative of fast ionic transport on the AC surface.

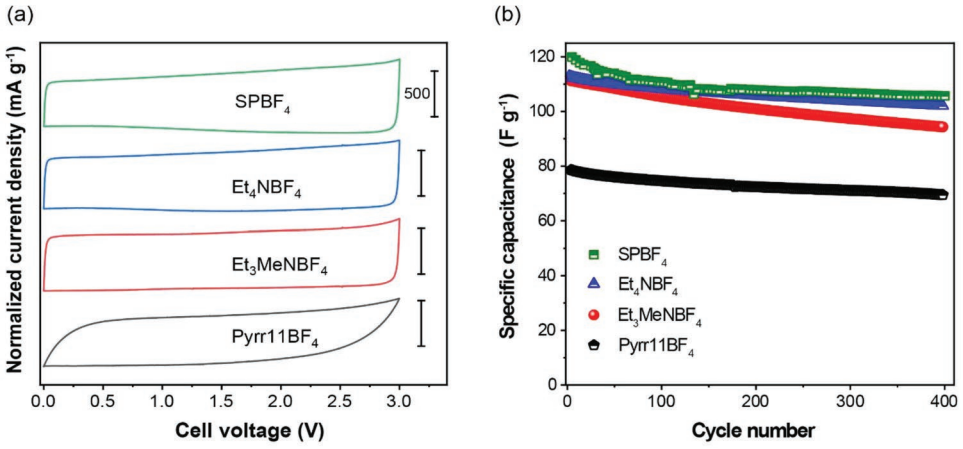

Figure 2. a) Cyclic voltammetry profiles of EDLCs in a solution consisting of acetonitrile and different organic salts ($SPBF_4$, Et_4NBF_4, Et_3MeNBF_4 and $Pyrr11BF_4$) at a concentration of 1.0 mol L^{-1}. The scan rate is 5 mV s^{-1}. b) Specific capacitance retention of EDLCs (under galvanostatic charge-discharge cycling) at 0.5 A g^{-1} for 400 cycles.

The specific capacitance stemmed from the cyclic voltammetry plots is given by the following equation[37,38]:

$$C\left(Fg^{-1}\right)=\frac{1000}{m\times v\times(\Delta V)}\int_{V_-}^{V_+}I(V)dV \tag{4}$$

where m is the active mass on one electrode, v is the scan rate, V_+ denotes the cathodic potential, V_- the anodic potential, and I represents the current response. The results are presented in Figure 2.

The normalized current densities are comparable, reaching 0.5 A g^{-1} at a scan rate of 5 mV s^{-1}. Likewise, the specific capacitances (C_{sp}) gleaned from the galvanostatic charge-discharge cycling (at 0.5 A g^{-1}) are similar and hinge on 109 F g^{-1} after 400 continuous cycles, showing a loss of 0.025% per cycle (Figure 2b). In general, the devices encompassing the $SPBF_4$ salt exhibit comparable performance with Et_3MeNBF_4 and Et_4NBF_4, compared to the ionic plastic $Pyrr11BF_4$ electrolyte,[25,26] where an inferior electrochemical performance (highlighted by the non-rectangularity of the CV and the resulting C_{sp} of 78 F g^{-1}) is attested.

Furthermore, the volumetric capacitance (C_{vol}) that stems from the electrolyte volume ($V_{electrolyte}$ = 0.0071 cm^{-3}) and bulk electrode density (d = 0.7 cm^3 g^{-1}), i.e., $C_{vol} = C_{sp} \times d$, spans between 56 to 76 F cm^{-3} (**Table 3**). The electrolyte-to-electrode volume ratio (Γ) defined as the ratio of the electrolyte volume to the total electrode volume reaches 21. This value appears high compared to the values used in industrial devices (e.g., $0.8 < \Gamma < 1.1$),[12] and is ascribed to the fact that coin-cell or Swagelok devices accommodate a large free volume. On the other hand, this free volume offers suitable conditions for gas generation during lab-scale experiments.

A good estimate of the number of free ions available in the electrolyte is given by the utilization factor (η, Table 3), described by the following equation [12]:

$$\eta=\frac{C_{vol}\times V_{max}\times N_e}{4\times Z_+\times Z_-\times C\times\Gamma\times\mathcal{N}_a} \tag{5}$$

where C_{vol} is the volumetric capacitance, V_{max} denotes the device maximum voltage, N_e describes the number of electrons per Coulomb, Z_+ and Z_- are the valences of the positive and negative ions in the electrolyte, $\mathcal{N}_a$ is Avogadro's constant, Γ expresses the electrolyte-to-electrode volume ratio and C represents the electrolyte concentration. Taking into account the charge distribution on the ions, the partial charges of Table 1 are used here to account for the Z_+ and Z_- values, yielding a corrected utilization factor (η'), in contrast with other studies[12] where the formal charge (±1) was introduced for the Z values (η).

Table 3. Utilization factor (η), and electrolyte-to-electrode volume ratio (Γ) values of the electrolytes comprising ACN and different organic salts, i.e., $SPBF_4$, Et_4NBF_4, Et_3MeNBF_4 and $Pyrr11BF_4$.

	$SPBF_4$	Et_4NBF_4	Et_3MeNBF_4	$Pyrr11BF_4$
C [mol L^{-1}]	1.0	1.0	1.0	4.0
C_{sp} [F g^{-1}]	109	107	98	80
C_{vol} [F cm^{-3}]	76.3	74.9	68.6	56
V_{max} [V]	3.0	3.0	3.0	3.0
Γ	21.0	21.13	21.13	21.13
$\lvert\delta^-\rvert$ for BF_4^-	0.50	0.50	0.50	0.50
$\lvert\delta^+\rvert$ for cations	0.13	0.09	0.14	0.23
η [%] with $Z_+ = Z_- = 1$	2.7	2.7	2.4	0.5
η' [%] with $Z_+ = \delta^+ = Z_- = \delta^-$	42.3	59.5	34.1	4.4

A more noticeable effect of the revised charge distribution on the utilization factor (η') is evident in Table 3. The fact that the utilization factor is limited by the cation is logical when considering that the studied cations are larger than the anion BF_4^- and holds a weaker partial charge. Furthermore, the η' values are larger aiding us to conclude the η' is largely in favour of the Et_4N^+ and SBP^+ compared to the $Pyrr^+$, despite the latter being smaller in size and having a higher concentration (×4). Besides, the relatively higher utilization factor η' values validate the ease of the ammonium and spiro cations to insert and disinsert from the AC micropores.

Investigating further the electrochemical characteristics of the $SPBF_4$/ACN electrolyte, cyclic voltammograms of the symmetric EDLCs are given in **Figures 3**a,b for two $SPBF_4$ concentrations, 0.5 and 1.0 mol L^{-1}. Higher concentrations were not investigated since greater amounts of BF_4^- generate larger gas volume.[39,40] The high degree of rectangularity at 5 mV s^{-1} (the grey dotted lines in Figures 3a,b represent ideal capacitive behavior) irrespective of the voltage window (1.5 → 3.0 V) connotes an essentially capacitive process associated with the formation of the EDL.[41] At this timeframe, the ions in the electrolyte are accessible to a more significant portion of the activated carbon pores. At higher scan rates (>50 mV s^{-1}, Figure S4, Supporting Information), however, due to non-optimal ion-electrolyte interaction and the appearance of equivalent and parallel series resistances (ESR and EDR),[42] the EDL traits are altered, manifested by reduced specific capacitance values and lowered rectangularity. The linear range of the logarithm of the normalized current density (j) against the logarithm of the scan rate (v) yielded b values of ≈0.905 and 0.92 (Figure S5, Supporting Information) for 0.5 and 1.0 mol L^{-1} $SPBF_4$, respectively, indicative of a surface-controlled, reversible electron-ion adsorption mechanism. To be exact, a generic case where all present ions are solvated at a fully discharged state and solely contribute to the electrolyte conductivity, while counter-ion adsorption represents the primary charging mechanism (despite desolvation examples being reported in nanoporous carbons[43]).

Next, accelerated ageing floating tests were employed to investigate the device's stability. The cell capacitance was calculated from the slope of the discharge curve of the two-electrode EDLC via the following equation:

$$C=\frac{I}{\frac{dV}{dt}} \tag{6}$$

where C is the capacitance of the cell, I denotes the discharge current, and dV/dt denotes the slope of the discharge process. In a symmetrical two-electrode system, the active material

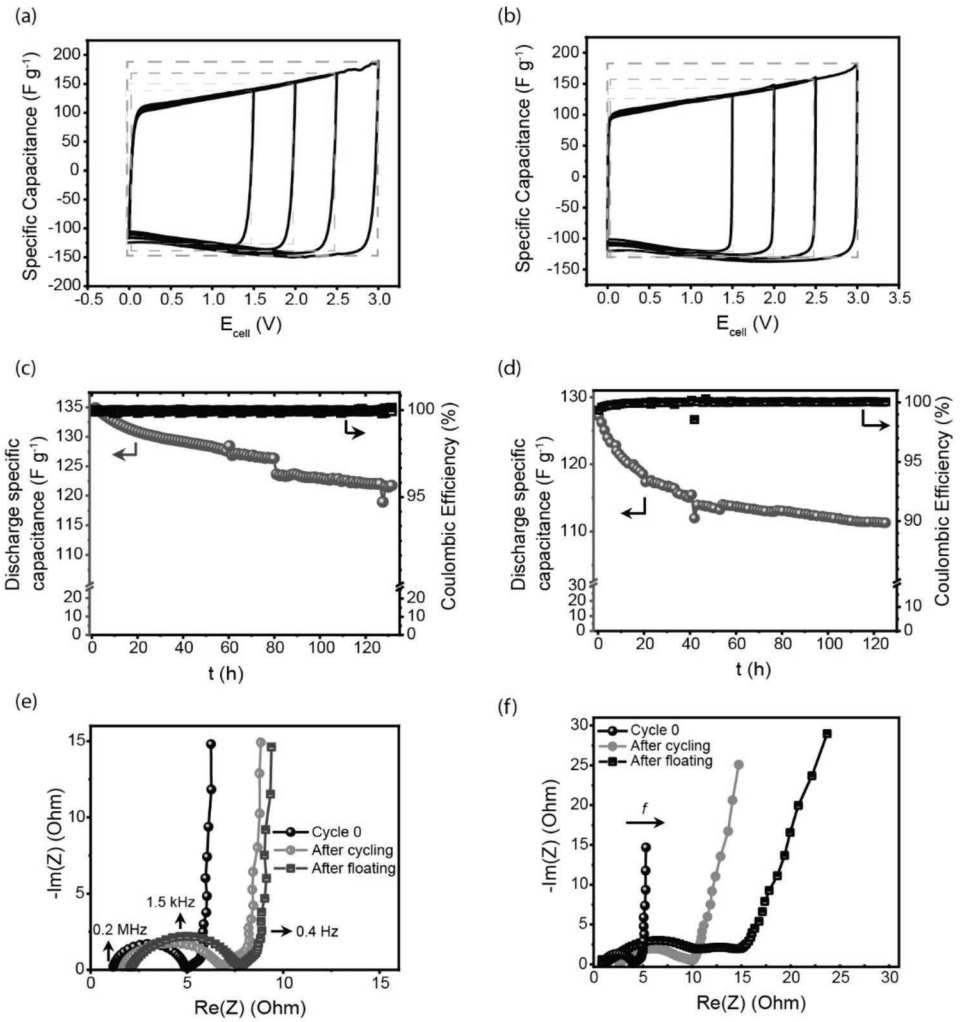

Figure 3. Electrochemical characterization of EDLCs containing 0.5 and 1.0 mol L^{-1} $SPBF_4$ and ACN. a,b) Cyclic voltammogram profiles at different cell voltages. c,d) Discharge-specific capacitance and coulombic efficiency during 125 h of floating tests. e,f) Nyquist plots before and after the floating tests.

weight is the same for both electrodes. The specific capacitance, C_{sp} (F g^{-1}) is related to the capacitance of the cell by[44]:

$$C_{sp} = \frac{2C}{m} \tag{7}$$

where C is the capacitance of the cell, and m describes the mass of the active material.

The specific capacitance extracted from the galvanostatic discharge curves (Figure S6a and S6b, Supporting Information) was initially 132 F g^{-1} for 0.5 mol L^{-1} $SPBF_4$ and 126 F g^{-1} for 1.0 mol L^{-1} $SPBF_4$. At the end of the floating protocol, C_{sp} shifted to 121 and 110.5 F g^{-1}, for 0.5 and 1.0 mol L^{-1} $SPBF_4$, respectively (Figures 3c,d), having an average specific capacitance loss of 0.12 F g^{-1} per hour. The coulombic efficiency lingers at 99% throughout the floating process.

Moreover, the ESR, which denotes the sum of electronic and ionic resistances of the EDLC, reaches 24 Ohm after commissioning and advances to 31 Ohm (19% increase) after the floating process (Figure S6c and S6d, Supporting Information). The Nyquist plots corroborate the growth of the ESR at longer floating timeframes. The semi-circle in the high-frequency region (0.2 MHz, Figure 3e,f) depicts the cell's internal resistance[45] ($R_{electronic}$, see Figure S6, Supporting Information for further details) and is visually enlarged after the floating process. At lower frequencies (0.4 Hz and onwards), a near-vertical line attests to the capacitive nature of the device.[23] It is important to note that the ESR values are slightly more significant for the device with the higher $SPBF_4$ content as the ionic resistance is a function of electrolyte conductivity and, in turn, concentration.

3.3. In Situ Gas Pressure Measurements of the AC-Based Symmetric EDLC

To reliably monitor the voltage-dependent gas evolution of an EDLC device, measurements directly probing the gas phase or registering the internal cell pressure are essential. The gas generation rate depends on the device's capacitance, temperature, and operating voltage. The measuring of the chemical composition of the gases (through chromatography) from different electrolytes at several operating voltages during various electrical operations

has been studied by several groups.[40,46–49] A more recent study combined gas pressure with standard electrical ageing data in packaged 100-F-size EDLCs (containing 1.0 mol L^{-1} Et_4NBF_4 in ACN) and revealed a relationship between gas pressure increase and electrical performance loss.[24] In this vein, through a custom-made cell[29] (Figure S7, Supporting Information), the instantaneous rate of pressure change ($\Delta P = \frac{dP}{dt}$) is examined during galvanostatic cycling and tailored to the rate of generation of gaseous products.

It should be noted that ΔP is comparable to the change of vapour pressure of the electrolyte (ACN) due to temperature variation.[50] More precisely, the value from the linear fitting of the pressure-temperature plot hits 3.336 mbar °C^{-1} (**Figure 4**a), while the ACN vapour pressure is ≈4.87 mbar °C^{-1} (it reaches 0.12 mbar at 298 K).[50] Thus, we correct this difference in our readings.

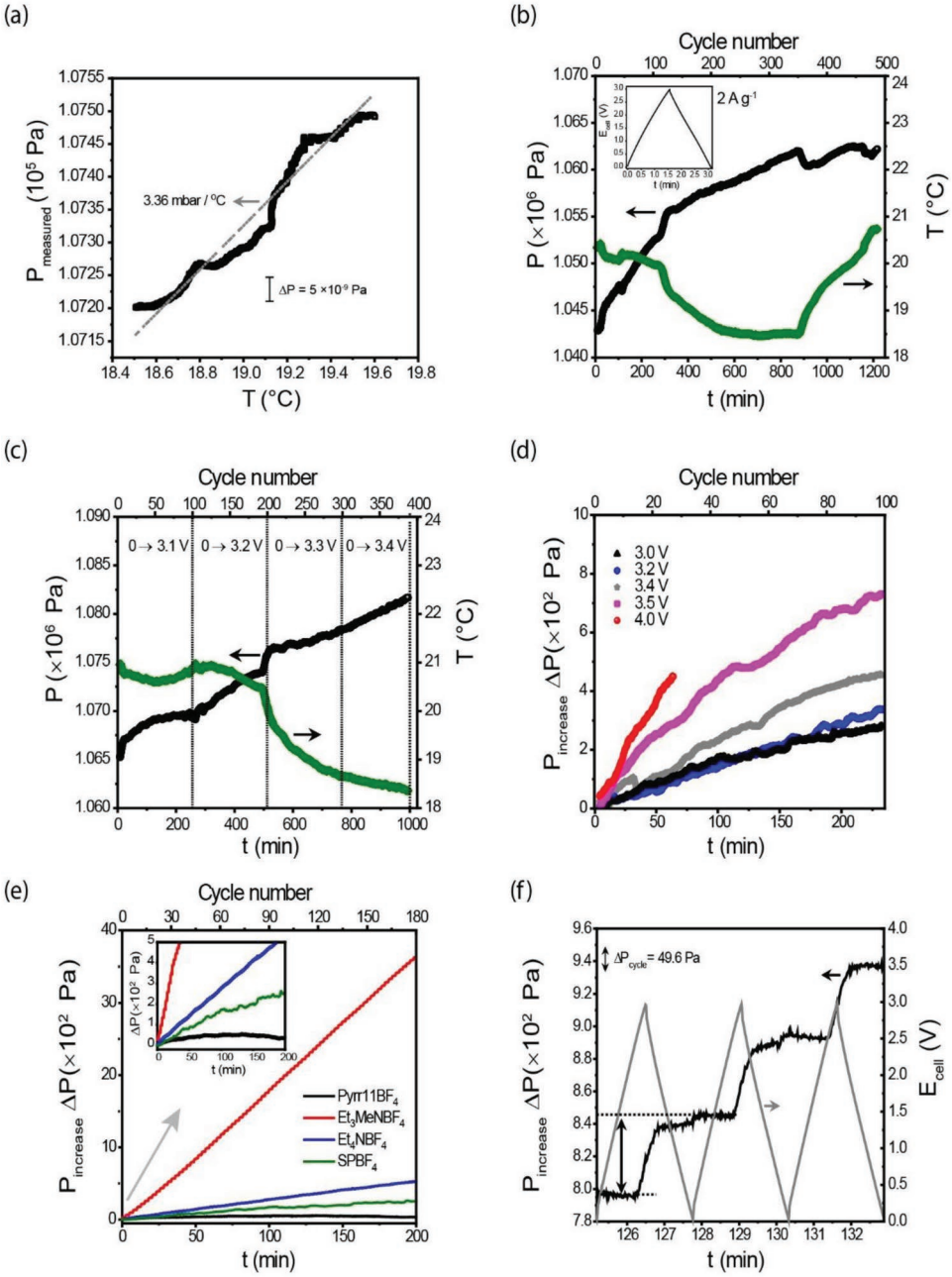

Figure 4. a) Vapour pressure variation with temperature at an idle state. The electrolyte comprises 1.0 mol L^{-1} $SPBF_4$ in ACN. b) In situ pressure evolution during GCD cycling along with the variation of temperature. Inset shows the GCD plot of an EDLC containing 1.0 mol L^{-1} $SPBF_4$ and ACN at 2.0 A g^{-1}. c) In situ pressure measurements of generated gasses during GCD cycling at different cell voltages. The right-hand x-axis describes the temperature variation upon cell operation. d) Relationship between the EDLC electrochemical window (in V) and the pressure generated from the cells when cycled for 230 min, under 2.0 A g^{-1}. e) Comparison of in situ pressure evolution of EDLCs under different organic salts at a 2.0 A g^{-1} and E_{cell} of 3 V. Inset shows the early stages of pressure evolution. (f) In situ pressure measurements of generated gasses during GCD cycling at 2.0 A g^{-1} in an EDLC under 1.0 mol L^{-1} Et_4NBF_4 in ACN.

Figure 4b shows the pressure increase with time (20 h, the equivalent of 500 cycles) of an EDLC operating at a current density of 2.0 A g^{-1} within 0 and 3.0 V. It shifted from 1.045 to 1.061×10^5 Pa, a slight increase of 2%, signifying the absence of electrolyte decomposition at this electrochemical window. Likewise, an insignificant increase in pressure (≈5%) was observed at voltages as high as 3.4 V (Figure 4c and Figure S8, Supporting Information), more significant than the potential of gas propagation on pure ACN, viz. 3.25 V.[23] As expected, gas evolution in the form of chemical and/or electrochemical gas consumption was detected at a cell operating voltage of 3.5 V and further up to 4.0 V, as illustrated in Figure 4d. ΔP increases four-fold (e.g., $0 \rightarrow 2 \times 10^2$ Pa at 3.5 V) under twenty cycles.

The self-decomposition of salt rather than solvent decomposition typically contributes to the most gases in the initial state of charge.[16] Then, the amount of gas evolution strongly depends on the material(s) used, in this case, the surface functionalities of the AC that act as catalytic sites or decompose themselves.[21,51] In this context, the formation of H_2, CO_2, and CO originates from the catalytic decomposition of carbon in contact with a dual-cation electrolyte[39,40] (i.e., lithium tetrafluoroborate $LiBF_4$/$SPBF_4$ in PC) or an aqueous lithium sulfate electrolyte[39] have been previously described. For the dual-cation electrolyte, H_2 stems from the excessive reduction of the negative electrode (lithium titanate oxide), whereas CO and CO_2 are byproducts of oxidation at the positive electrode (AC).[39,40]

Moreover, the gas evolution of the EDLC comprising 1.0 mol L^{-1} $SPBF_4$/ACN is inferior to the other organic salts, as illustrated in Figure 4e, aside from the plastic crystal $Pyr_{11}BF_4$, where negligible ΔP values are evidenced (i.e., ≈25 Pa). The $Pyr_{11}BF_4$/ACN system considerably reduces gas generation by attenuating localized heating thanks to its plastic crystal character,[52] as opposed to ammonium cations that exacerbate this effect. The stability of the quaternary salts varying with the steric barriers through Hofmann elimination renders Et_4N^+ and Et_3MeN^+ more susceptible to decomposition than the SBP^+.[39,40]

For the case of Et_4NBF_4 (Figure 4f), a noticeable pressure increase (49.6 Pa) is apparent during the charging process. The different electrode/electrolyte interfacial characteristics during the cell's operation are manifested by a localized increase in temperature coming from the generation of instantaneous heat at each electrode.[53] The latter is associated with the nature of the electrolyte and, in turn, the ability of the ions to desolvate. It has been identified by in-operando calorimetry on aqueous and organic electrolytes[53] and deep eutectic solvents,[28] where exothermic Joule heating occurs during charging due to ion adsorption, similar to the finding of Figure 4f. The Joule reversible heating at the AC (negative electrode) during the beginning of the charging process is caused by the desolvation of pyrrolidinium cations as they enter the activated carbon pores.[53]

4. Conclusion

An essential characteristic of an electrolyte is the solubility of the solvent since its high conductivity offers the EDLC a low internal resistance and high current output. By a priori analyzing the physicochemical properties of the $SPBF_4$/ACN electrolyte, comparing it with an Et_4NBF_4/ACN analogue and establishing the electrochemical behavior of four organic salts (i.e., $SPBF_4$, Et_4NBF_4, Et_3MeNBF_4, $Pyrr11NBF_4$), this study focuses on the safety aspect of EDLCs manifested by real-time gas evolution monitoring under ambient conditions during long-term galvanostatic cycling. The results highlight that these devices containing the organic ionic plastic crystal $Pyr11BF_4$ display a marginal pressure increase (≈25 Pa) compared to the ones comprising asymmetric and acyclic tetrafluoroborate salts, albeit with poor electrochemical performance. For the $SPBF_4$/ACN electrolyte, a more pertinent comparison at different voltages (3.0 → 4.0 V) revealed moderate gas generation up to 3.4 V (≈190 Pa at 3.0 V, that shifts to ≈400 Pa at 3.4 V) owing to a stable AC/electrolyte interface and a severe one after 3.5 V, primarily stemming from the electrolyte decomposition. Nonetheless, the results of this study benchmark an operating voltage of 3.4 V for safe and long-term cell operation in the presence of 1.0 mol L^1 $SPBF_4$/ACN (yielding a specific capacitance of 110 F g^{-1}), where a balance between the ability to break solvent-cation interactions, the electrochemical stability, the localized heating, and the amount of gas formed holds.

Supporting Information

Supporting Information is available from the Wiley Online Library or from the author.

Acknowledgements

The authors would like to thank "La Région Centre Val de Loire" for financial support.

Conflict of Interest

The authors declare no conflict of interest.

Data Availability Statement

The data that support the findings of this study are available in the supplementary material of this article.

Keywords

acetonitrile, activated carbon, EDLC, gas formation, ionicity, spiro

Received: September 15, 2022
Revised: October 5, 2022
Published online:

[1] A. Ray, B. Saruhan, *Materials.* **2021**, *14*, 2942.
[2] X. Yang, M. Li, N. Guo, M. Yan, R. Yang, F. Wang, *RSC Adv.* **2016**, *6*, 4365.
[3] F. Barzegar, D. Y. Momodu, O. O. Fashedemi, A. Bello, J. K. Dangbegnon, N. Manyala, *RSC Adv.* **2015**, *5*, 107482.
[4] B. E. Conway, *Electrochemical supercapacitors: scientific fundamentals and technological applications*, Springer Science & Business Media, New York **1999**.

[5] G. Nikiforidis, M. Anouti, *Batteries Supercaps* **2021**, *4*, 1708.
[6] E. J. Brandon, M. C. Smart, W. C. West, *J. Mater. Res.* **2020**, *35*, 113.
[7] R. R. Galimzyanov, S. V. Stakhanova, I. S. Krechetov, A. T. Kalashnik, M. V. Astakhov, A. V. Lisitsin, A. Y. Rychagov, T. R. Galimzyanov, F. S. Tabarov, *J Power Sources* **2021**, *495*, 229442.
[8] T. Han, M.-S. Park, J. Kim, J. H. Kim, K. Kim, *Chem. Sci.* **2016**, *7*, 1791.
[9] H. V. T. Nguyen, K. Kwak, K.-K. Lee, *Electrochim. Acta* **2019**, *299*, 98.
[10] Y. Chikaoka, E. Iwama, M. Sakurai, T. Ueda, T. Shirane, W. Naoi, K. Naoi, *J. Phys. Chem.* **2021**, *125*, 5995.
[11] X. W. Yu, D. B. Ruan, C. C. Wu, J. Wang, Z. Q. Shi, *J. Power Sources* **2014**, *265*, 309.
[12] S. Jayaraman, T. J. Rawson, M. A. Belyustina, *Energy Environ. Sci.* **2022**, *15*, 2948.
[13] M. M. Amaral, R. Venâncio, A. C. Peterlevitz, H. Zanin, *J. Energy Chem.* **2022**, *67*, 697.
[14] J. Chmiola, G. Yushin, Y. Gogotsi, C. Portet, P. Simon, P. L. Taberna, *Science* **2006**, *313*, 1760.
[15] D. DeRosa, S. Higashiya, A. Schulz, M. Rane-Fondacaro, P. Haldar, *J Power Sources* **2017**, *360*, 41.
[16] P. Liu, M. Verbrugge, S. Soukiazian, *J. Power Sources* **2006**, *156*, 712.
[17] F. Cheng, X. Yu, J. Wang, Z. Shi, C. Wu, *Electrochim. Acta.* **2016**, *200*, 106.
[18] S. Park, K. Kim, *J Power Sources* **2017**, *338*, 129.
[19] M. Sevilla, A. B. Fuertes, *ACS Nano* **2014**, *8*, 5069.
[20] D. Yiğit, M. Güllü, T. Yumak, A. Sınağ, *J. Mater. Chem.* **2014**, *2*, 6512.
[21] P. Ruschhaupt, S. Pohlmann, A. Varzi, S. Passerini, *Batteries Supercaps* **2020**, *3*, 698.
[22] J. Li, Z. Xu, Z. Zhang, *RSC Adv.* **2018**, *8*, 32188.
[23] G. Nikiforidis, M. E. Yagoubi, M. Anouti, *Electrochim. Acta* **2022**, *402*, 139529.
[24] J. R. Miller, S. Butler, *J Power Sources* **2021**, *509*, 230366.
[25] J. M. Pringle, J. Adebahr, D. R. MacFarlane, M. Forsyth, *Phys. Chem. Chem. Phys.* **2010**, *12*, 7234.
[26] S. Forsyth, J. Golding, D. R. MacFarlane, M. Forsyth, *Electrochim. Acta* **2001**, *46*, 1753.
[27] B. Gorska, L. Timperman, M. Anouti, F. Beguin, *Phys. Chem. Chem. Phys.* **2017**, *19*, 11173.
[28] S. Phadke, S. Amara, M. Anouti, *Chemphyschem* **2017**, *18*, 2364.
[29] S. Phadke, M. Anouti, *Electrochim. Acta* **2017**, *223*, 31.
[30] M. Raghibi, B. Xiong, S. Phadke, M. Anouti, *Electrochim. Acta* **2020**, *362*, 137214.
[31] M. Petrowsky, R. Frech, *J. Phys. Chem. B* **2010**, *114*, 8600.
[32] J. Masa, S. Barwe, C. Andronescu, W. Schuhmann, *Eur. J. Chem.* **2019**, *25*, 158.
[33] Z. Wang, A. Hofmann, T. Hanemann, *Data Brief* **2019**, *23*, 103703.
[34] S. Kim, J. Wee, K. Peters, H.-Y. S. Huang, *J. Phys. Chem.* **2018**, *122*, 5280.
[35] J. A. Riddick, W. B. Bunger, T. K. Sakano, *Organic solvents: physical properties and methods of purification*, 4th ed., John Wiley and Sons, New York **1986**.
[36] H. V. T. Nguyen, S. Lee, K. Kwak, K.-K. Lee, *Electrochim. Acta* **2019**, *321*, 134649.
[37] G. Nikiforidis, S. Wustoni, C. Routier, A. Hama, A. Koklu, A. Saleh, N. Steiner, V. Druet, H. Fiumelli, S. Inal, *Macromol. Biosci.* **2020**, *20*, 2000215.
[38] J. Chidiac, G. Nikiforidis, L. Timperman, M. Anouti, *Chemphyschem* **2022**, *23*, e202200224.
[39] Q. Gao, L. Demarconnay, E. Raymundo-Piñero, F. Béguin, *Energy Environ. Sci.* **2012**, *5*, 9611.
[40] Y. Chikaoka, E. Iwama, S. Seto, Y. Okuno, T. Shirane, T. Ueda, W. Naoi, M. T. H. Reid, K. Naoi, *Electrochim. Acta* **2021**, *368*, 137619.
[41] G. Nikiforidis, S. Wustoni, D. Ohayon, V. Druet, S. Inal, *ACS Appl. Energy Mater.* **2020**, *3*, 7896.
[42] D. Boonpakdee, C. F. Guajardo Yévenes, W. Surareungchai, C. La-o-vorakiat, *J. Mater. Chem.* **2018**, *6*, 7162.
[43] A. C. Forse, C. Merlet, J. M. Griffin, C. P. Grey, *J. Am. Chem. Soc.* **2016**, *138*, 5731.
[44] S. Wustoni, G. Nikiforidis, S. Inal, Y. S. Indartono, V. Suendo, B. Yuliarto, *APL Mater.* **2022**, *10*, 061101.
[45] S. Amara, W. Zaidi, L. Timperman, G. Nikiforidis, M. Anouti, *J. Chem. Phys.* **2021**, *154*, 164708.
[46] E. Iwama, T. Ueda, Y. Ishihara, K. Ohshima, W. Naoi, M. T. H. Reid, K. Naoi, *Electrochim. Acta* **2019**, *301*, 312.
[47] Y.-Y. Park, H. Tomiyasu, H. Atarashi, Y. Sugibayashi, M. Saito, N. Asanuma, *Electrochemistry* **2020**, *88*, 99.
[48] J. Menzel, E. Frąckowiak, K. Fic, *Electrochim. Acta* **2020**, *332*, 135435.
[49] M. He, K. Fic, E. Frąckowiak, P. Novák, E. J. Berg, *ChemElectroChem* **2019**, *6*, 566.
[50] J. Safarov, M. Geppert-Rybczyńska, E. Hassel, A. Heintz, *J. Chem. Thermodyn.* **2012**, *47*, 56.
[51] M. Hahn, A. Würsig, R. Gallay, P. Novák, R. Kötz, *Electrochem. Commun.* **2005**, *7*, 925.
[52] L. Köps, F. A. Kreth, A. Bothe, A. Balducci, *Energy Storage Mater.* **2022**, *44*, 66.
[53] A. Likitchatchawankun, G. Whang, J. Lau, O. Munteshari, B. Dunn, L. Pilon, *Electrochim. Acta* **2020**, *338*, 135802.